Developmental Cell, Volume *54*

Supplemental Information

Buckling of an Epithelium Growing under Spherical Confinement

Anastasiya Trushko, Ilaria Di Meglio, Aziza Merzouki, Carles Blanch-Mercader, Shada Abuhattum, Jochen Guck, Kevin Alessandri, Pierre Nassoy, Karsten Kruse, Bastien Chopard, and Aurélien Roux

Supplementary Figures S1-S7

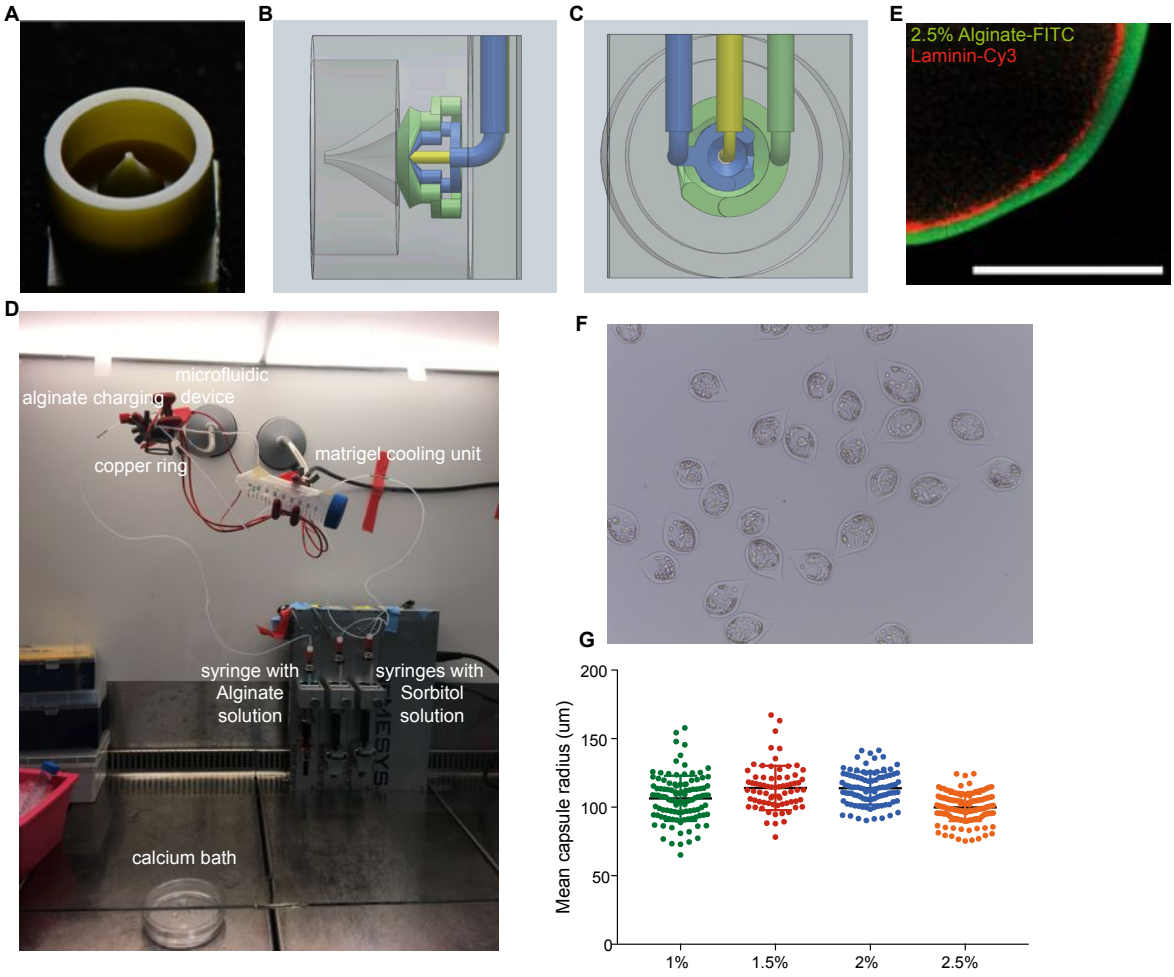

FIG. S1: **3d-printed microfluidic device and cell encapsulation experimental setup.** Related to Fig. 1. **A,** 3D-printed microfluidic device. **B,** draft of the side view of the microfluidic device. The green, blue and yellow colors represent alginate, sorbitol solution and cell solution flows, respectively. **C,** draft of the back view of the microfluidic device. The green, blue and yellow colors represent alginate, sorbitol solution and cell solution flows, respectively. **D,** a photo of the experimental setup. **E,** Phase-contrast microscope image of 2.5% alginate capsule with growing epithelial monolayers, at 24h after capsule formation. **F,** Box-plot of mean capsule radius as a function of alginate solution percentage.

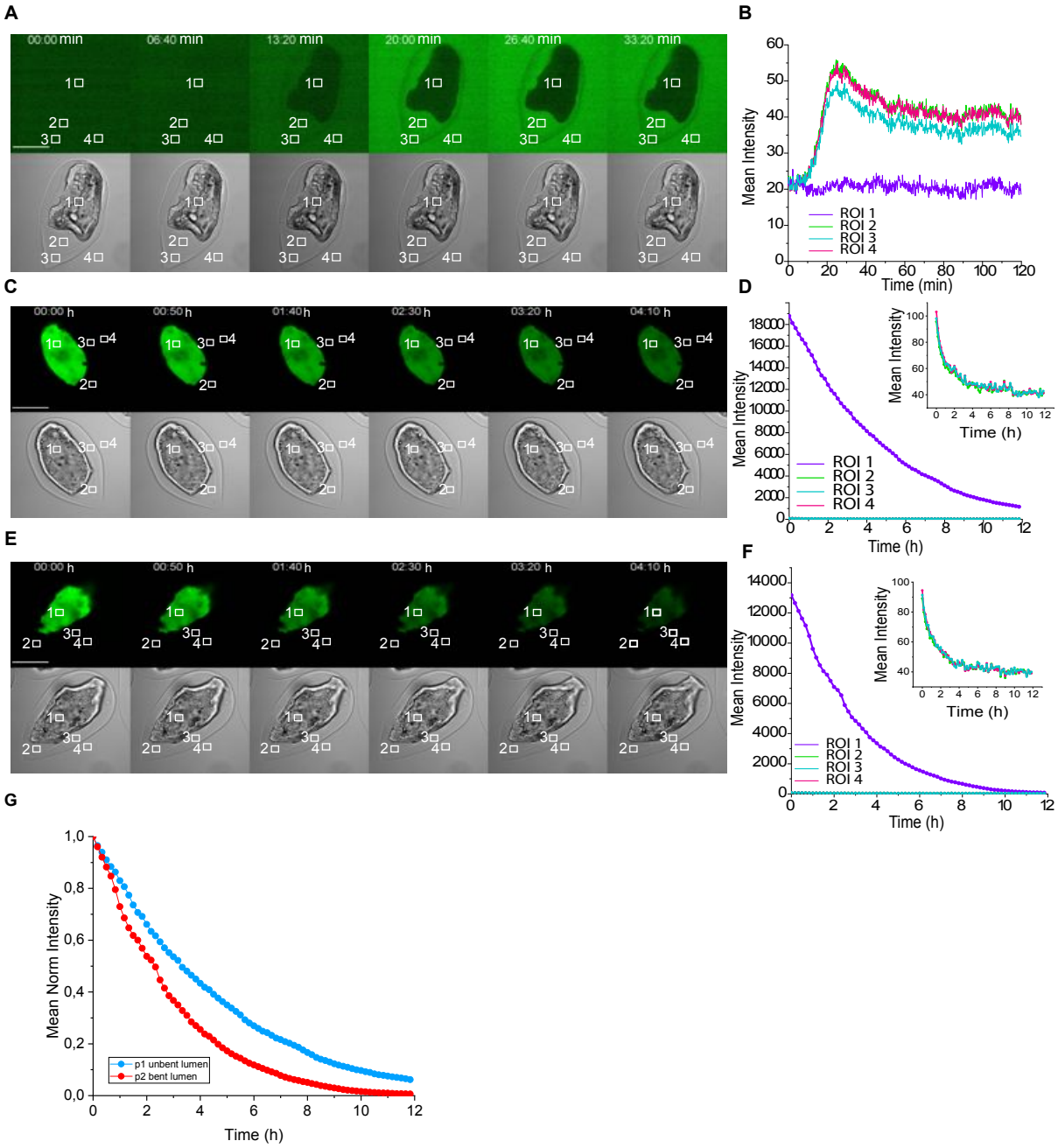

FIG. S2: **Capsule permeability and monolayer integrity controls.** Related to Fig. 2. **A,** FITC diffusion from exterior to interior of a capsule. Top; FITC image of a confocal scan of a capsule equatorial plane containing buckled MDCK mCherry-ActinH2B-GFP monolayer. Bottom; Transmitted light image of the same capsule. **B,** Dependence of mean fluorescence intensity over time for ROIs depicted on **A**. **C,** FITC diffusion from interior to exterior of a capsule. Top; FITC image of a confocal scan of a capsule equatorial plane containing not yet buckled MDCK mCherry-ActinH2B-GFP monolayer. Bottom; Transmitted light image of the same capsule. **D,** Dependence of mean fluorescence intensity over time for ROIs depicted on **C**. **E,** FITC diffusion from interior to exterior of a capsule. Top; FITC image of a confocal scan of a capsule equatorial plane containing buckled MDCK mCherry-ActinH2B-GFP monolayer. Bottom; Transmitted light image of the same capsule. **F,** Dependence of mean fluorescence intensity over time for ROIs depicted on **E**. **G,** Mean normalised fluorescence intensity as a function of time for both ROIs 3 (corresponding to the ROI in the monolayer lumen) at **C** and **E**. Scale bars, 100 μm.

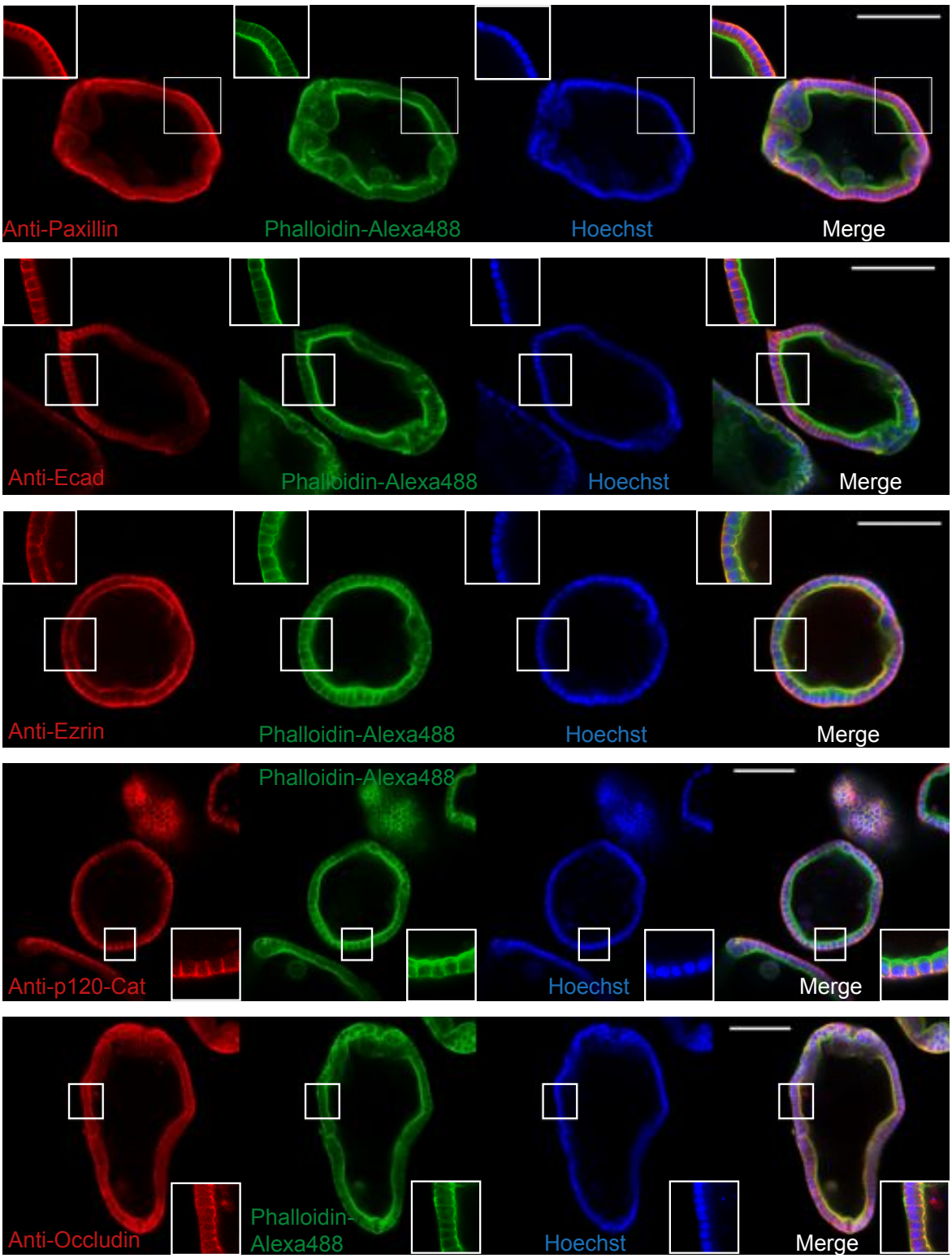

FIG. S3: **Confocal scans of immunostained formed monolayers.** Related to Fig. 2. MDCK monolayers were fixed and immunostained to see the distribution Paxillin, Ecadherin, Ezrin, p120-Catanine and Occludin proteins. Nuclei were stained with Hoechst and filamentous actin with Phalloidin-Alexa488. Scale bars, 100 μm.

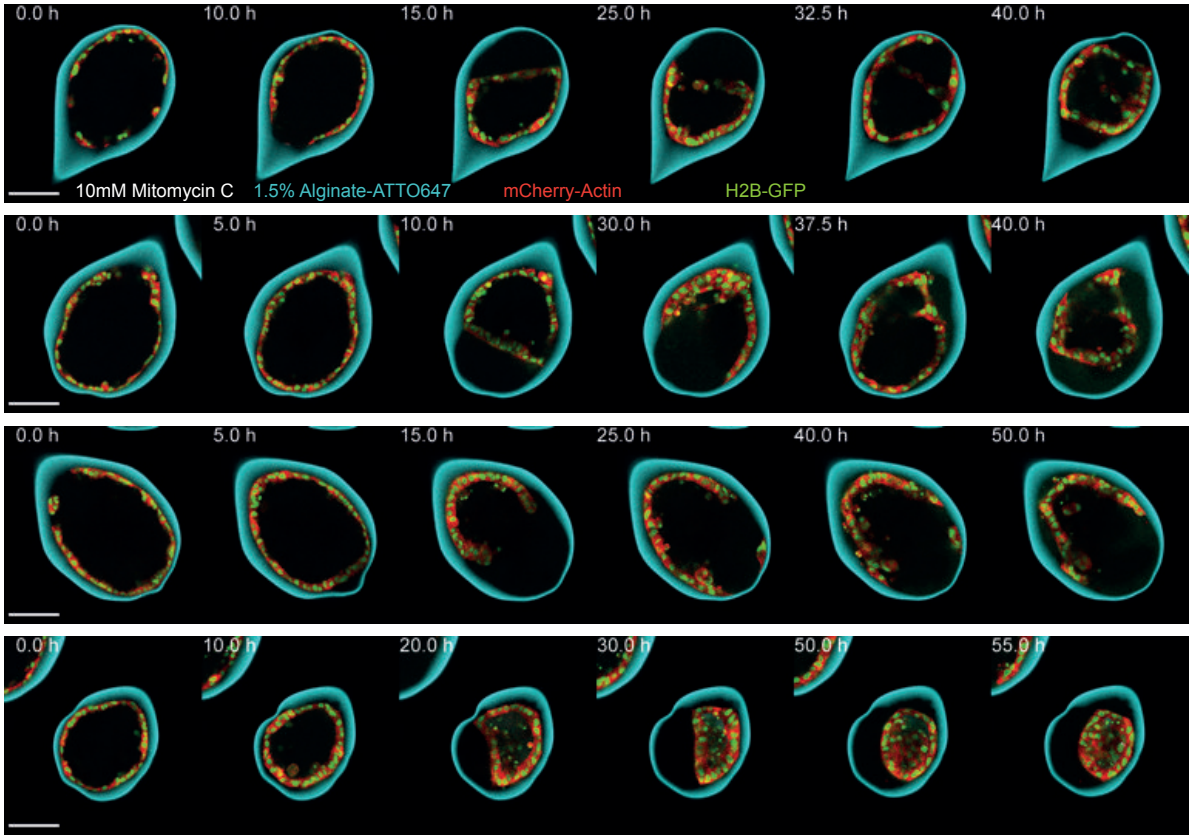

FIG. S4: **Confocal equatorial planes of MDCK mCherry-ActinH2B-GFP monolayers treated with** 10 μ**M Mitomycin-C.** Related to Fig. 2. Scale bars, 100 μm.

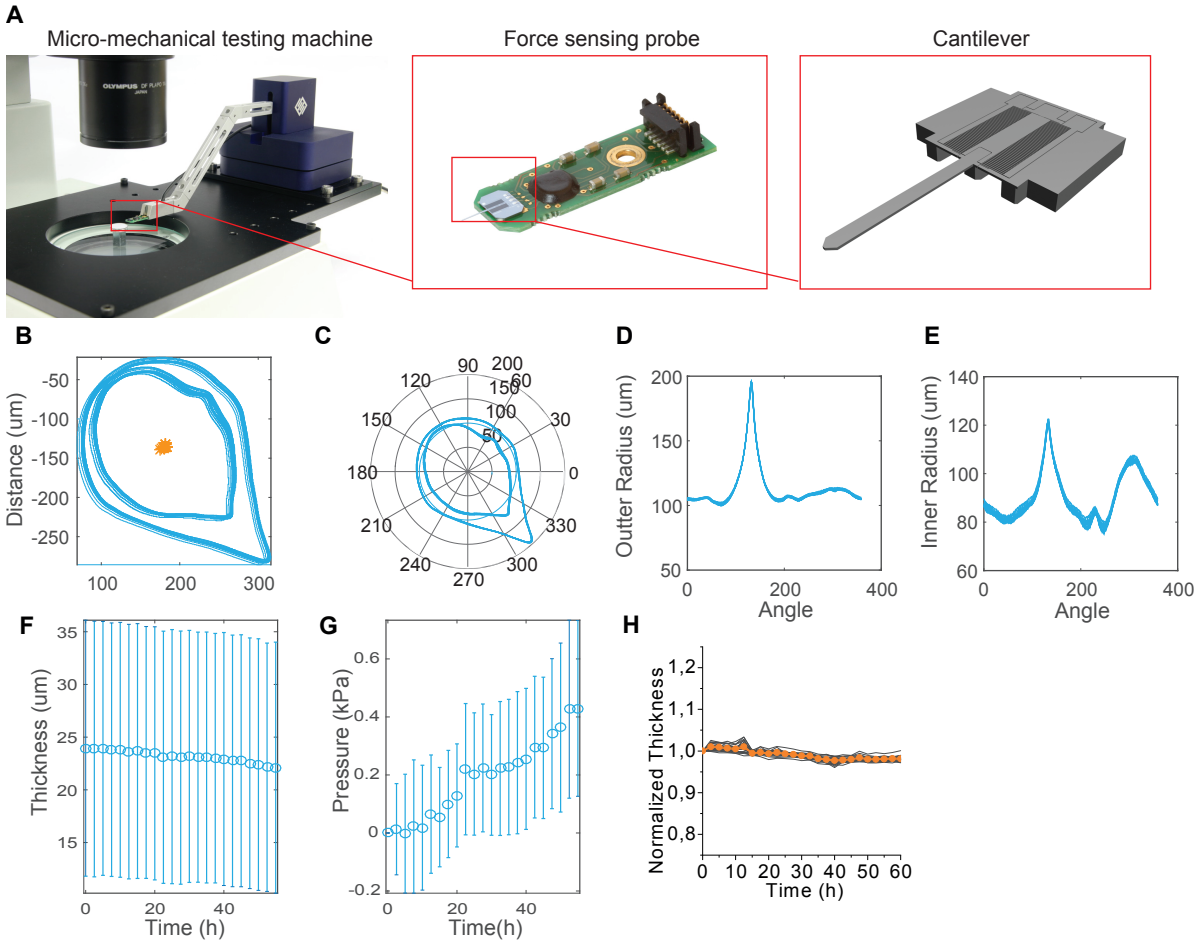

FIG. S5: **Measurement procedures of buckling pressure, fold opening angle, fold depth, and consecutive fold angle position.** Related to Fig. 3. **A,** FemtoTools micro-mechanical testing machine. **B,** superimposed capsule contours of inner and outer boundaries corresponding to different time points. **C,** superimposed capsule contours of inner and outer boundaries corresponding to different time points in polar coordinates with the origin at capsule inner surface centroid. **D,** superimposed plots of outer capsule radii as a function of polar angle corresponding to different time points. The radii correspond to the outer contours in **C**. **E,** superimposed plots of inner capsule radii as a function of polar angle corresponding to different time points. The radii correspond to the inner contours on c. **F,** mean capsule thickness as a function of time for the contours in **C**. Each point represents a mean of 360 capsule thickness measurements corresponding to 360 angles of polar coordinates. Error bars are SDs. **G,** mean capsule pressure as a function of time for the contours in **C**. Each point represents a mean of 360 capsule pressures measurements corresponding to 360 angles of polar coordinates. Error bars are SDs. **H,** Normalized mean capsule thickness as a function of time for empty capsules (i.e. without cells) made of 2.5% alginate solution; n=22; error bars are SEMs. Scale bars, 100 μm.

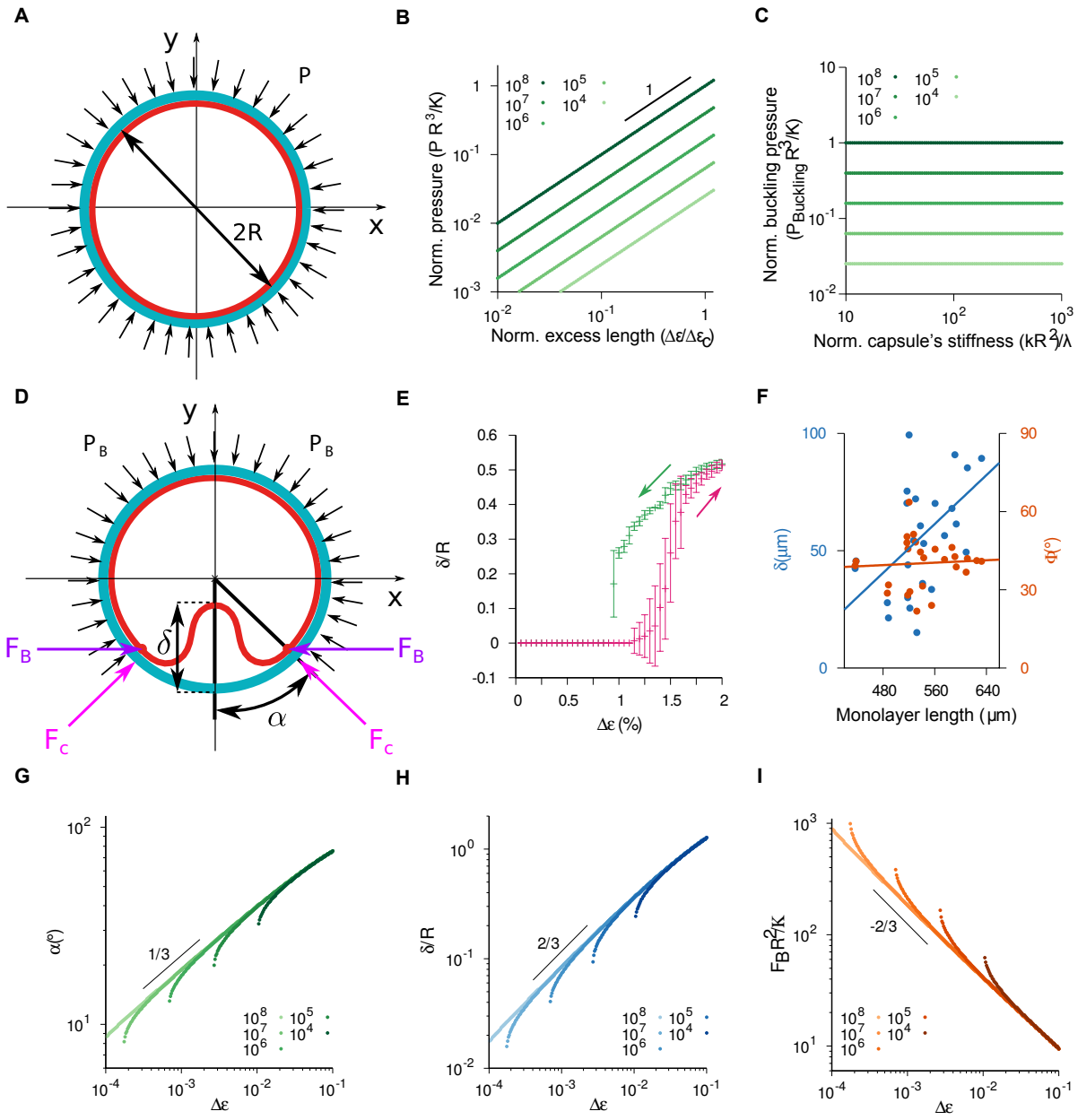

FIG. S6: **Characteristics of a confined elastic ring across the buckling instability.** Related to Fig. 4. **A,** Schematic of a compressed elastic ring (red) under the pressure P of the confinement ring (cyan). R is the radius of the confinement. **B,** Normalized pressure ($PR^3/\mathcal{K}$) as a function of the ratio between the excess strain ($\Delta\epsilon$) and the critical excess strain ($\Delta\epsilon_c$) before the buckling instability (Eq. S25 for $\lambda R^2/\mathcal{K} \gg 1$) for values of the normalized compressional rigidity ($\lambda R^2/\mathcal{K}$) between 10^4 and 10^8. The critical excess strain is given by Eq. S21. **C,** Normalized buckling pressure ($P_{\text{Buckling}}R^3/\mathcal{K}$) as a function of the normalized capsule stiffness (kR^2/λ) for the same compressional rigidity values as in panel **B**. P_{Buckling} is given by Eq. S26. **D,** Schematic of a buckled elastic ring (red) under the pressure P_B of the confinement ring (cyan). The buckled segment is characterized by its height δ and its opening angle α. Both forces $F_C = P_B R \tan(\alpha)$ and $F_B = P_B R/\cos(\alpha)$ relate to the pressure P_B. **E,** Fold height δ as a function of the excess strain $\Delta\epsilon$. Magenta (Green) curve corresponds to δ of stationary shapes for an increasing (decreasing) ramp of $\Delta\epsilon$ from 0% (2%) to 2% (0%) at regular intervals of 0.05%. Initial conditions correspond to the stationary shape at the preceding excess strain with small amplitude fluctuations. Set of parameters: $\mathcal{K} = 10^{-2}$, $\lambda = 10^2$, $k = 10^5$ and $R = 1$. Error bars are SD with N=30. **F,** Experimental values of δ and Φ as a function of the length of monolayers with one fold. Solid lines are linear fits. **G-I**, Opening angle α, fold height δ/R and force $F_B R^2/\mathcal{K}$ as a function of the excess strain $\Delta\epsilon$, respectively. For each panel, each curve corresponds to a distinct value of the normalized compressional rigidity ($\lambda R^2/\mathcal{K}$) between 10^4 and 10^8 as indicated in the legends.

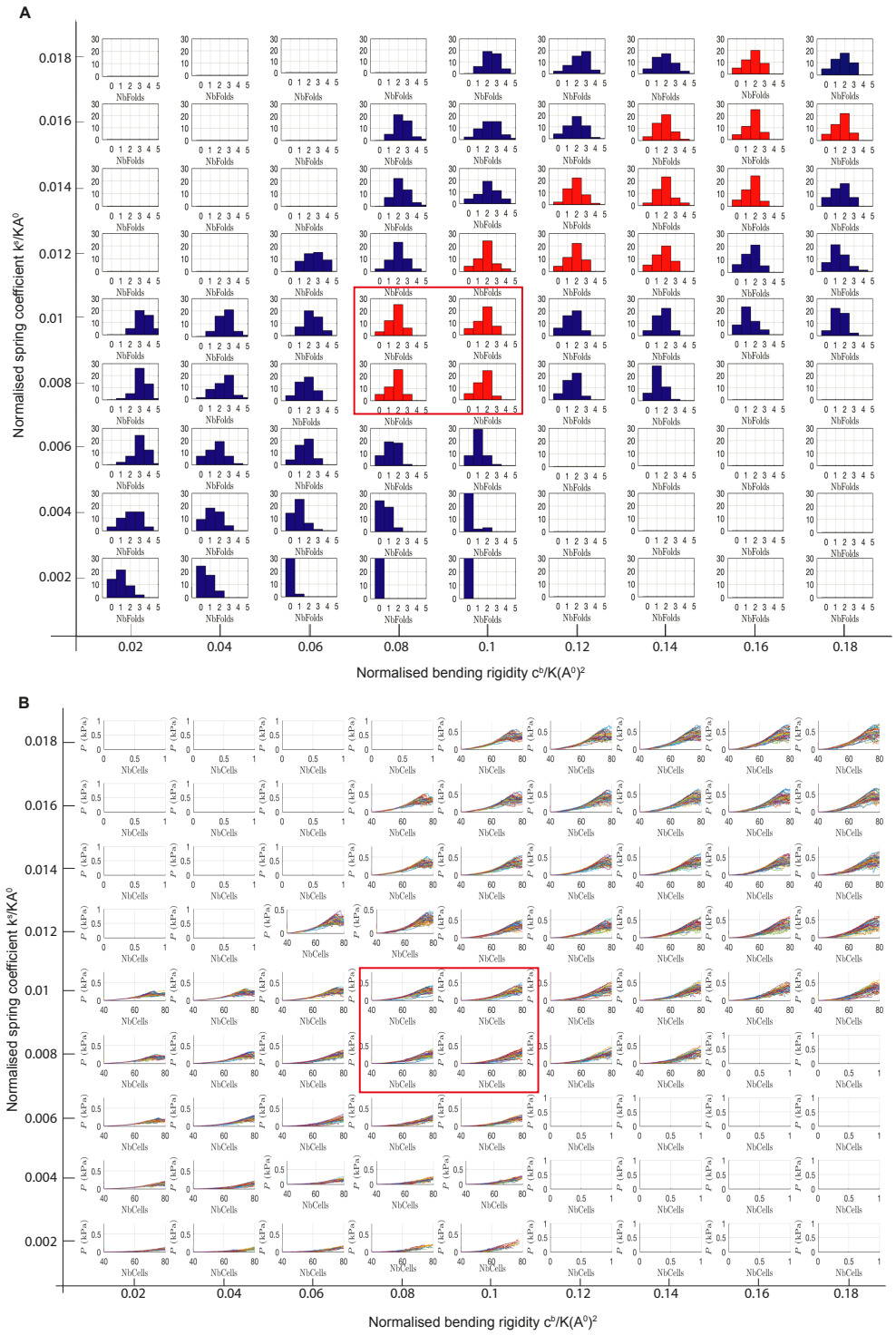

FIG. S7: **Tissue buckling within different parameter regions.** Related to Fig. 5. **A,** Distribution of the number of folds as a function of the normalised spring coefficient k^s/KA^0 and the normalised bending rigidity $c^b/K(A^0)^2$. The parameter regions where the distribution of number of folds match the experimental observations are coloured in red. **B,** Pressure evolution within different parameter regions. Evolution over time (the number of cells increase from 40 to 80) of the pressure P applied by the growing tissue on the elastic capsule within different parameter regions (k^s/KA^0 and $c^b/K(A^0)^2$). In both panels, the red square marks the parameters regime that fits best experiments.

Method S1. Theoretical and Numerical appendix. Related to Fig 4, 5 and 6

Section 1: Estimation of the water flux across a monolayer upon folding

In the following, we estimate the flux of small molecules across a monolayer and compare its value with measurements for epithelial monolayers.

The volume of a monolayer lumen (i.e. hollow space enclosed by the monolayer) is estimated by considering that a monolayer lumen is a sphere with a radius $R \sim 100$ μm. Hence its volume is of the order of $V \sim 4 \cdot 10^{-12}$ m^3. Similarly, the area of a monolayer lumen can be estimated by assuming a spherical geometry with the same characteristics as above, yielding an area of the order of $A \sim 10^{-7}$ m^2. Next, we consider that over the $T \sim 2$ h ~ 7000 s that folding lasts, a monolayer lumen loses half of its volume due to a water outflow J across the surface of the monolayer lumen. Therefore, this water outflow is of the order of

$$J = \frac{V/2}{AT} \sim 2 \cdot 10^{-9} \text{ m/s}. \tag{S1}$$

Of note, the premise that the total volume lost is half of the initial volume is in general an overestimation, according to our experiments. Previous measurements of small-molecule fluxes across epithelial monolayers in other contexts range between $10^{-6} - 10^{-8}$ m/s, depending on the molecule type (Rosenthal et al, 2019, p. e13334; Rosenthal et al, 2010, pp. 1913-1921). This suggests that water evacuation from the lumen to the exterior is not hindering the kinetics of monolayer folding.

Section 2: Description of a confined elastic ring (macroscopic approach)

In this section, we introduce a description for the mechanics of epithelial monolayers weakly adhered to the inner surface of an elastic spherical shell. In particular, we focus our attention on the understanding of the tissue dynamics near the transition between a spherical state into a buckled state.

Alginate capsules act as rigid containers that constrain the growth of tissues. To a good approximation in our setting (see main text), alginate capsules are regarded as thin linear elastic materials with a Young's modulus $E \sim 20$ kPa, a thickness $h \sim 20$ μm and a Poisson ratio $\nu = 1/2$. Hence, in the thin-layer limit, alginate capsules are akin to elastic shells with bending rigidity $\mathcal{K}^{cap} = Eh^3/12(1-\nu^2)$ and compressional rigidity $\lambda^{cap} = Eh/(1-\nu^2)$ (Landau and Lifshitz, 1975, Theory of elasticity). These material parameters are of the order of $\mathcal{K}^{cap} = 20$ μN$\cdot\mu$m and $\lambda^{cap} = 0.5$ μN/μm, according to the parameter set in Table 1 in the main text.

Epithelial monolayers are active materials with the capacity to spontaneously undergo morphological changes regulated by cell forces. When confined to flat surfaces, epithelial cells often reach a confluent state in which the cell density plateaus and cell motion is drastically reduced, similar to glass phases of dense active particle suspensions. Since the experimental analysis is done for a confocal slice, we describe the cell layer as a cylindrical shell and assume translational invariance along the cylinder axis. Unless otherwise stated, we consider only the cross section of the cylinder and look at deformations of a ring. The lack of cell flows at the onset of the buckling transition suggests that the complex mechanics of encapsulated epithelial monolayers can be approximated by a $2d$ thin elastic ring. Unlike alginate capsules, their bending rigidity $\mathcal{K}$ and compressional rigidity λ are regarded as independent material parameters a priori, which might be regulated through cell-cell adhesion, cell-matrigel adhesion or cell contractility. Therefore the global energy per unit length of the $2d$ system constituted by the monolayer and the capsule reads

$$\mathcal{E} = \mathcal{K} \int_L \kappa^2 ds + \lambda \int_{L_0} \left(\left| \frac{\partial \mathbf{r}}{\partial s_0} \right| - 1 \right)^2 ds_0 + k \int_L (|\mathbf{r}| - R)^2 H(|\mathbf{r}| - R) ds, \tag{S2}$$

The first term represents bending energy with κ being the local mean curvature in $2d$. The second term represents the strain energy where the integrand stands for the relative displacement between two material points with respect to their equilibrium configuration. The third term represents the adhesion-free interaction between the tissue and the capsule. For small capsule deformations, this interaction is approximated by a piece-wise harmonic potential with a spring constant k dependent on the material properties of the capsule, where $H(|\mathbf{r}| - R)$ is a Heaviside step function and R is the radius of the alginate capsules (see Fig. 4 in the main text). The current elastic-ring shape is parametrized by the arc-length s with its length being L, whilst the equilibrium elastic-ring shape in the absence of constraints is parametrized by the arc-length s_0 with its length being L_0.

The area of the monolayer is found experimentally to increase over time as a result of cell proliferation. The observed linear growth in cell number yields a doubling time scale of about ~ 60 hours. Remarkably, this time scale is significantly larger than the time scale of buckling formation ~ 10 hours, suggesting that L_0 variations can be ignored during tissue folding dynamics as a first order approximation. The separation of these two time scales enables to decouple the dynamics driven by cell division to the mechanical relaxation of cellular forces. Thereby, as a simplifying approximation we assume that the system equilibrates before large density variations occur and presume that the resting length L_0 is a time-independent parameter. The effects induced by the competition between cell proliferation and cell mechanics relaxation time scales is discussed elsewhere. Therefore taking as unit length R and as energy unit $\mathcal{K}/R$, the mechanics of elastic-ring folding are fully characterized by three dimensionless parameters: the elastic-ring compressional rigidity $\lambda R^2/\mathcal{K}$, the capsule spring constant $kR^4/\mathcal{K}$ and the ratio between the elastic-ring length and the capsule length $L_0/2\pi R$.

Numerical methods

The details of the numerical method employed to study the statistical properties of our system are as follows: at a given instant of time, the state of an elastic ring is described by the position of N material points which are located at positions $\mathbf{r}_i = (x_i, y_i)$ with $i \in (0, N-1)$. Typically, $N = 100$. The energy per unit length assigned to a certain configuration is given by the discretized form of the mechanical energy (S2), namely

$$\mathcal{E}^*([x_i, y_i]) = \mathcal{K} \sum_{i=0}^{N-1} \kappa_i^2 |\Delta \mathbf{r}_i| + \lambda \sum_{i=0}^{N-1} \frac{(|\Delta \mathbf{r}_i| - L_0/N)^2}{L_0/N} + k \sum_{i=0}^{N-1} (|\mathbf{r}_i| - R)^2 H(|\mathbf{r}_i| - R) |\Delta \mathbf{r}_i|, \tag{S3}$$

where $|\mathbf{r}_i| = \sqrt{x_i^2 + y_i^2}$, $|\Delta \mathbf{r}_i| = \sqrt{(x_{i+1} - x_i)^2 + (y_{i+1} - y_i)^2}$ and $\kappa_i = 4((y_{i+1} - 2y_i + y_{i-1})(x_{i+1} - x_{i-1}) - (x_{i+1} - 2x_i + x_{i-1})(y_{i+1} - y_{i-1}))/((x_{i+1} - x_{i-1})^2 + (y_{i+1} - y_{i-1})^2)^{3/2}$ is the curvature at the i-th position. Because of the ring geometry $x_N = x_0$ and $y_N = y_0$.

To compute the configurations with minimal energy, we introduce an artificial dissipative dynamics that drives the system toward a local minimum of the energy (S3). For each material point dynamics is determined by

$$\frac{d\mathbf{r}_i}{dt} = -\frac{1}{\tau \mathcal{K}/R} \frac{\partial \mathcal{E}^*}{\partial \mathbf{r}_i} \quad \text{for } i \in [0, N-1] \tag{S4}$$

For us, the time scale τ is arbitrary and thus, it is set to $\tau = 1$. Notice that the system might be trapped in metastable states in the absence of bulk fluctuations.

Section 3: Buckling instability induced by confinement elasticity

In the present section, we revisit the problem of an inextensible elastic ring introduced inside an undeformable rigid circular ring. This problem has been investigated to various degrees and in different ways by a number of researchers: see for instance (Lo et al, 1962, pp. 691-695; Chan and McMinn, 1966, pp. 433-442) in the main text.

For simplicity, we focus first in the limit of inextensible rings and underformable confinements, meaning that $\lambda/\mathcal{K}R^2, k/\mathcal{K}R^4 \gg 1$ in Eq. S2. Thereby the elastic-ring forces are neither sufficient to deform capsules nor to compress/extend material elements (i.e. $L = L_0$). We solve numerically Eq. S3 to obtain the equilibrium shapes. When the monolayer length is smaller than the length of the capsule ($L_0/2\pi R \leq 1$), the elastic ring attains a circular shape regardless of the confinement as there are no contact interactions between them. When the ring length is larger than the length of the confinement ($L_0/2\pi R > 1$), however a buckling instability occurs. Note that elastics rings attain a shape with a single fold induced by geometrical confinement.

To investigate further the emergence of a buckled ring shape above a certain length L_0, we study analytically the behaviour of elastic rings near the transition point. To this end, we propose to account for the morphological variations as the system undergoes the buckling transition by the following parametrization for the ring shape

$$r(\theta) = R\left(1 - \frac{\delta}{1 + (\sin(\theta - \theta_i)/\alpha)^2}\right), \tag{S5}$$

where r and θ are the radial and angular coordinate with respect to the confinement center of mass, respectively. In cartesian coordinates, the shape curve is parametrized as $(x(\theta), y(\theta)) = (r(\theta)\cos(\theta), r(\theta)\sin(\theta))$. For $\delta \neq 0$, the ring

exhibits a folded region located at the random angular position θ_i. Its shape is characterized by two coefficients: δ that controls the fold amplitude and α that controls its angular width.

The length of an inextensible ring parametrized by Eq. S5

$$L_0 = \int_0^{2\pi} \sqrt{(x(\theta)')^2 + (y(\theta)')^2} d\theta \tag{S6}$$

is a conserved quantity. Considering that the coefficients $\delta, \alpha \ll 1$, the leading order corrections in δ and α of Eq. S6 can be recast as

$$L_0 = 2\pi R \left(1 + \frac{\delta^2}{8\alpha} - \delta\alpha\right) \tag{S7}$$

By defining the excess strain $\Delta\epsilon = \Delta L/2\pi R$ as the excess length $\Delta L = L_0 - 2\pi R$ of the ring with respect to the confinement perimeter normalized by the latter, Eq. S7 can be expressed as

$$\Delta\epsilon = \frac{\delta^2}{8\alpha} - \delta\alpha. \tag{S8}$$

Likewise, the bending energy of an inextensible ring parametrised by Eq. S5 is expressed as

$$\mathcal{E} = \mathcal{K} \int_0^{2\pi} \kappa^2 \sqrt{(x(\theta)')^2 + (y(\theta)')^2} d\theta, \tag{S9}$$

where the local curvature reads $\kappa = (y(\theta)''x(\theta)' - y(\theta)'x(\theta)'')/((x(\theta)')^2 + (y(\theta)')^2)^{3/2}$. Up to leading order corrections in δ and α, Eq. S9 can be recast as

$$\mathcal{E} = \frac{2\pi\mathcal{K}}{R}\left(1 + \frac{3\delta^2}{4\alpha^3}\right), \tag{S10}$$

Combining Eqs. S8,S10 and calculating the shape that minimizes the energy (S10) with the geometrical constraint given by Eq. S8, we deduce power-law relations between the geometrical properties of the buckled ring (δ, α) and its current excess strain $\Delta\epsilon$, which read

$$\delta = 4(5/2)^{1/3}\Delta\epsilon^{2/3} \tag{S11}$$

$$\alpha = (2/5)^{1/3}\Delta\epsilon^{1/3} \tag{S12}$$

As $\Delta\epsilon$ increases progressively beyond the value at the buckling transition, both parametric coefficients increase but the relative variation of them is different. We predict that for the same variation in L_0, the amplitude of the fold δ increases more than the angular width α, thereby conditioning tissue growth.

The sub-linear variations of the energy per unit length of the minimal buckled shape against the excess strain read

$$\frac{\mathcal{E} - 2\pi\mathcal{K}/R}{2\pi\mathcal{K}/R} = 30 \cdot (5/2)^{2/3}\Delta\epsilon^{1/3}, \tag{S13}$$

Equilibrium number of folds at the buckling instability

Here we present an argument to show that the minimal shape near the buckling transition exhibits at most one prominent fold. To address this question, we follow a similar argument as above and parametrize a ring shape with n equal folds by the function

$$r(\theta) = R\left(1 - \sum_{i=1}^{n} \frac{\delta}{1 + (\sin(\theta - \theta_i)/\alpha)^2}\right). \tag{S14}$$

We ignore geometrical heterogeneities among folds as presumably they would lead to configurations with overall higher mechanical energies. Remember that r and θ are the radial and angular coordinate with respect to the capsule's geometrical center, respectively. For $\delta \neq 0$, the shape is buckled n times at the angular positions $\theta_1, ..., \theta_n$ with the distance between two consecutive folds $\theta_{i+1} - \theta_i = 2\pi R/n$ being constant.

As we introduced above, when the excess strain $\Delta\epsilon = (L_0 - 2\pi R)/2\pi R \ll 1$, the deformations of the ring shape are expected to be small as well, meaning that both parametric coefficients $\delta, \alpha \ll 1$. In this situation, we can cast the leading corrections of the length L_0, which is constant for inextensible elastic rings, as follows

$$\Delta\epsilon = n\left(\frac{\delta^2}{8\alpha} - \delta\alpha\right). \tag{S15}$$

Notice that the excess strain of a ring with n folds is simply given by the excess strain of a single fold (S8) times the number of folds n, as expected from mean-field considerations. Similarly, the correction to the total energy per unit length (S2) near the buckling transition also scale linearly with the number of folds and it reads

$$\frac{\mathcal{E} - 2\pi\mathcal{K}/R}{2\pi\mathcal{K}/R} = n\frac{3\delta^2}{4\alpha^3}. \tag{S16}$$

Combining Eqs. S15-S16 and calculating the minimum of (S16) with the geometrical constraint given by Eq. S15, we deduce the power-law relations between the geometrical properties of the buckled ring (δ, α) and its excess strain $\Delta\epsilon$ and number of folds n, which read

$$\delta = 4(5/2)^{1/3}(\Delta\epsilon/n)^{2/3} \tag{S17}$$
$$\alpha = (2/5)^{1/3}(\Delta\epsilon/n)^{1/3} \tag{S18}$$

In contrast to the ring length L_0 Eq. S15 , the geometrical properties of the fold are not proportional to the number of folds. Both parametric coefficients follows a power law with the number of folds n and the exponent is smaller than 1. From the expression of δ and α, the energy per unit length of the minimal buckled shapes becomes

$$\frac{\mathcal{E} - 2\pi\mathcal{K}/R}{2\pi\mathcal{K}/R} = 30 \cdot (5/2)^{2/3} n^{2/3} \Delta\epsilon^{1/3}. \tag{S19}$$

Remarkably, the energy increases with the number of folds n in a sublinear manner. As a result, the shape with overall minimal energy has one fold for small excess strain $\Delta\epsilon \ll 1$.

Asymptotic limits of the buckling transition for confined elastic rings

In the sections above, we focus our study in the ideal limit of an inextensible elastic ring and rigid capsules to understand the mechanics of buckled tissues under confinement. However, the compressibility of epithelial cells can not be disregarded in our setting, as prior to the buckling transition, cell shape variations are observed. These observations suggest that cells have a finite compressional rigidity λ whose value is estimated from experimental measurements of capsule elastic deformations (see Table 1 in the main text). In the present section, we explore how the buckling transition is influenced by the capsule and tissue rigidities.

In the general situation, two limiting cases can be distinguished for elastic-ring deformations controlled by the rigidity of capsules. When comparing the energetic contribution attributed to elastic-ring and capsule deformations in Eq. S2, a dimensionless parameter emerges λ/kR^2. Hence, the tissue growth is influenced by the ratio between the cellular compressional rigidity λ and the stiffness of the capsule k. Notice that the spring constant k relates to the material properties of the capsule such that $k = \lambda^{cap}/R^2$, as it is discussed in the section below. In consequence, the dimensionless parameter λ/kR^2 is independent of the capsule radius R, but not of capsule and cell mechanics.

For $\lambda/kR^2 \ll 1$, the deformations of cell shapes are energetically favorable against capsule deformations, meaning that below the buckling transition, cells tend to accommodate the internal stress generated by cell proliferation through shape deformations. As a consequence, when cells are compliant, the threshold of the buckling transition is set by balancing bending and compressional cell deformations. In particular, for $\lambda R^2/\mathcal{K} \ll 1$ cells are infinitely compressible, so that the excess strain $\Delta\epsilon$ is fully accommodated through cell compression. In this situation, the minimal shape of the elastic ring is a circle of radius R and the leading correction of the total energy per unit length as a function of the small excess strain $\Delta\epsilon = (L_0 - 2\pi R)/2\pi R \ll 1$ reads

$$\mathcal{E} - 2\pi\mathcal{K}/R = \lambda(2\pi R)\Delta\epsilon^2. \tag{S20}$$

Alternatively, the limit of inextensible elastic rings (i.e. $\lambda R^2/\mathcal{K} \gg 1$) yields an energy per unit length of the minimal buckled ring that is given by Eq. S13. The boundary between these two regimes can be delimited by comparing both energies (S13) and (S20), setting a critical excess strain

$$\Delta\epsilon_c^{5/3} = 30 \cdot (5/2)^{2/3}\frac{\mathcal{K}}{\lambda R^2}. \tag{S21}$$

Next, we further investigate the influence of tissue elastic parameters on the buckling transition. We numerically compute minimal shapes as a function of the excess strain $\Delta\epsilon$ and the dimensionless parameter $\mathcal{K}/\lambda R^2$. Fig. 4e in the main text shows two distinct morphological patterns for elastic rings, corresponding to circular rings and buckled rings. The critical excess strain $\Delta\epsilon_c$ given by Eq. (S21) is in qualitative agreement with numerical simulations. Consequently, when $\Delta\epsilon < \Delta\epsilon_c$, the ring attains a compressed circular shape of radius R, but for $\Delta\epsilon > \Delta\epsilon_c$, the ring buckles.

Next, we investigate the nature of the buckling transition by studying the stability of minimal shapes of Eq. S2 near the transition point. To this end, we numerically compute minimal shapes as a function of the excess strain $\Delta\epsilon$ for a fixed set of elastic parameters. The excess strain $\Delta\epsilon$, first increases from 0 to 0.02 and second decreases from 0.02 to 0 at regular intervals of 0.0005. At a certain $\Delta\epsilon$, the initial condition corresponds to the stationary shape at the preceding excess strain plus small amplitude fluctuations. Fig. S6e shows the height of the folded region of an elastic ring δ as a function of the excess strain, being $\delta = 0$ for circular rings and $\delta \neq 0$ for buckled rings. We observe signatures of hysteresis that is characteristic of first order transitions. The threshold for the increasing ramp of $\Delta\epsilon$ is not coincident with the threshold on the decreasing ramp, delimiting a coexistence region for intermediate excess strains, that in addition is manifested by larger error bars. We checked that the hysteresis region is robust to variations in the elastic parameters. Therefore, we conclude that the nature of the buckling transition is first order.

For $\lambda/kR^2 \gg 1$, the deformations of the capsule are energetically favourable against cell deformations, meaning that below the buckling transition, cells tend to expand and deform the capsule to accommodate the forces generated by cell proliferation. As a consequence, when capsules are compliant, the threshold of the buckling transition is set by balancing cell bending deformations and capsule compressional deformations. In particular, for $kR^4/\mathcal{K} \ll 1$ the capsules are infinitely compressible, so that the excess strain $\Delta\epsilon$ is fully accommodated through capsule inflation. In this situation, the minimal shape of the elastic ring is a circle of radius $L_0/2\pi > R$ and the leading correction of the total energy per unit length as a function of the small excess strain $\Delta\epsilon = (L_0 - 2\pi R)/2\pi R \ll 1$ reads

$$\mathcal{E} - 2\pi\mathcal{K}/R = k(2\pi R^3)\Delta\epsilon^2. \tag{S22}$$

In a similar spirit as above, the energy per unit length given by Eq. S13 for an inextensible ring inside an undeformable capsule can be employed to estimate the boundary between these two limiting cases, which sets the critical value for the excess length

$$\Delta\epsilon_c^{5/3} = 30 \cdot (5/2)^{2/3} \frac{\mathcal{K}}{kR^4}. \tag{S23}$$

Consequently, when $\Delta\epsilon < \Delta\epsilon_c$, the ring attains a circular shape of radius $L_0/2\pi > R$, but for $\Delta\epsilon > \Delta\epsilon_c$, the ring buckles.

Section 4: Forces of the ring-confinement system

In our setting, we can investigate the interplay between spherical alginate capsules and the morphological changes of epithelial tissues, and how these in turn are driven by the mechanical forces generated at the interface between capsules and cells. Indeed, epithelial monolayers can build up large-scale collective forces mediated by cell-cell contacts. These forces suffice to induce large deformations on capsules with elastic modulus of ~ 10 kPa. In the course of tissue buckling, distinct modes of deformations are identified. In the present section, we summarize the analytical arguments used to estimate the tissue forces from capsule deformations.

Isotropic pressure of an elastic ring before buckling

At the early stages, cells migrate freely on the inner surface of alginate capsules. Upon reaching a confluent state, in which no free spaces remain across the monolayer, cells keep on replicating and thus generating local force dipole at each of these events. The equilibration of these forces at the tissue-scale lead to an overall cellular compression, evidenced by the observed progressive increase of cell height or decrease of cell in-plane area. These compressive forces are transmitted to the substrate underneath, resulting in a measurable expansion of the alginate capsule. This first phase terminates, when the tissue folds.

To investigate the nature of the forces before buckling, let us consider a $3d$ elastic shell of radius $R + \delta R > R$ with $\delta R \ll 1$ that is confined in a shell of smaller radius R under the action of a uniform pressure P, Fig. S6a. The departure of the capsule from its equilibrium state is balanced by the work done by an external pressure P

Fig. S6a. The variation of the curvature in the compressed state is $\sim \delta R/R^2$, and the total bending energy scales as $\mathcal{K}(\delta R/R^2)^2R^2$. Besides the total stretching energy is $\lambda(\delta R/R)^2R^2$, where the strain on single cells scales as $\sim \delta R/R$. These elastic deformations are a consequence of the external compressional pressure P that represents the constraining forces by the alginate capsules, and so the total work supplied to the elastic ring is $\sim PR^2\delta R$. The ring deformations are computed through the minimization of the total energy

$$\mathcal{E} \sim \mathcal{K}(\delta R/R^2)^2R^2 + \lambda(\delta R/R)^2R^2 - PR^2\delta R, \tag{S24}$$

with respect to δR, yielding the compressive pressure as a function of the excess strain $\Delta\epsilon = \delta R/R$

$$P \propto \frac{\lambda\Delta\epsilon}{R}\left(1 + \frac{\mathcal{K}}{\lambda R^2}\right) \tag{S25}$$

in terms of the geometrical and mechanical properties of the elastic ring.

For the parameter set in Table 1 in the main text, the term $\mathcal{K}/\lambda R^2 \ll 1$ is negligible, meaning that Eq. S25 is further simplified to $P \propto \lambda\delta R/R^2$ for epithelial monolayers. Thereby, at the buckling transition for epithelia the excess strain $\Delta\epsilon \sim \Delta\epsilon_c$ takes the value given by Eq. S21, and thus the pressure at buckling reads

$$P_{\text{buckling}} \propto \frac{\lambda^{2/5}\mathcal{K}^{3/5}}{R^{11/5}}. \tag{S26}$$

Similar arguments can be used to obtain the harmonic interaction between the elastic ring and the confinement in Eq. S2 and in particular the scaling of the spring constant k with the material properties of alginate capsules. Through similar arguments the reactive force of alginate capsules to an expanding internal pressure P^* can be computed, leading to an equivalent result to Eq. S25, except that the mechanics of the capsule are probed instead of the ring mechanics and the displacement δR is outwards. Consequently Eq. S25 turns into

$$P^* \propto \frac{\lambda^{cap}\delta R}{R^2}\left(1 + \frac{\mathcal{K}^{cap}}{\lambda^{cap}R^2}\right), \tag{S27}$$

for a $3d$ spherical capsule confronted to an internal expanding pressure P^*. In consequence as we anticipated in Eq. S2, the capsule behavior resembles an harmonic potential with a spring constant $k = \lambda^{cap}/R^2(1 + \mathcal{K}^{cap}/\lambda^{cap}R^2)$, which according to the parameter set in Table 1 in the main text can be further approximated to $k \sim \lambda^{cap}/R^2$.

Forces between confinement and an elastic ring after buckling

At the intermediate stages, the compressional forces accumulation results in a buckling transition, in which a macroscopic part of the tissue detaches from the inner surface of the capsule and folds. From this point on, the buckled tissue is not in physical contact with the capsule, except for a thin region at the edge through which compressive forces from the capsule may stabilize the tissue shape.

To further investigate the interplay between the buckled tissue and the compressional forces at the contact region, we assume that the tissue behaves as a $2d$ thin elastic ring with a bending modulus $\mathcal{K}$ and compressional modulus λ. The following results has been reported previously elsewhere, (Chan and McMinn, 1966, pp. 433-442) in the main text. Here we revisit them in the context of tissue mechanics, but for more details about the intermediate calculations we refer to the original reference (Chan and McMinn, 1966, pp. 433-442) in the main text.

Let us consider a buckled elastic ring as illustrate in Fig. S6d, where the depth of the buckled ring is δ and the opening angle α. When adhesion is neglected, the part of the confinement in contact with the unbuckled segment of the ring withstands a uniform pressure P_B and a pair of normal forces per unit length $F_c = P_B R\tan\alpha$ at the contact points (red dots in Fig. S6d). These forces condition the shape of the inner elastic ring. In particular, enforcing force balance at the level of the contact points of the inner ring, results in a pair of compressive forces per unit length along the x-axis applied on the ends of the buckled ring, whose amplitude depends on the confinement-based forces through $F_B = P_B R/\cos\alpha$. These external forces applied to the buckled ring cancel out, however, they are sufficient to buckle the ring and stabilize its shape. Therefore, the local force balance equation for a material element of the buckled ring reads

$$\mathcal{K}\frac{d^2\phi}{ds^2} = -F_B\sin\phi, \tag{S28}$$

where ϕ is the angle between the tangent unit vector and the x-axis and s is the arc-length of the equilibrium shape. Thanks to the symmetry of the shape at the plane $x = 0$, the boundary conditions can be expressed as

$$\phi(s = 0) = 0, \tag{S29}$$

$$\phi(s = S^*) = \alpha, \tag{S30}$$

where $2S^*$ is the length of the buckled ring and 2α is the opening angle, Fig S6d. These set of equations determine a unique solution for ϕ, which is a complicated function of α, S^* and F_B. However these physical quantities are not independent, but they are related to the excess strain of the elastic ring $\Delta\epsilon = (L - 2\pi R)/2\pi R$ through conditions of self-consistency. In particular, at the contact points we enforce continuity of the curvature (i.e. $d\phi/ds = 1/R$) and continuity of the buckled ring $(x(s = S^*), y(s = S^*)) = (\sin\alpha, \cos\alpha)$. Lastly, the excess strain is the sum of the axial strain of the unbuckled part and the difference in length of the buckled part compared with the original arc

$$\Delta\epsilon = \left(1 - \frac{\alpha}{\pi}\right)\frac{F_B\cos\alpha}{\lambda} + \frac{F_B\sin\alpha}{\pi\lambda} + \left(\frac{S^*}{\pi R} - \frac{\alpha}{\pi}\right). \tag{S31}$$

Notice that for $\lambda \to \infty$, we recover the expected result for an inextensible ring.

For a given excess strain $\Delta\epsilon$ and λ, there is a unique shape of the buckled ring that obeys all these conditions. These relations are transcendental and thus not analytically solvable. In Fig. S6g-i, we summarize some of the relevant geometrical properties of the buckled shape as a function $\Delta\epsilon$ and $\lambda R^2/\mathcal{K}$: from left to right the depth of the buckled ring δ, the opening angle α and the dimensionless buckling forces $F_B R^2/\mathcal{K}$. All of them obey a power-law with the excess strain $\Delta\epsilon$ and most remarkably to a good approximation they are independent of the compressional modulus λ. Consequently, the shape of the buckled ring provides a simple readout of the dimensionless mechanical forces at the contact line $F_B R^2/\mathcal{K}$.

Here, we detail the fitting method used to construct Figs. 4h-i in the main text. As explained above, by enforcing force balance, we obtain the triad of parameters $(\alpha, \delta/R, P_B R^3/\mathcal{K}\cos\alpha)$ as a function of $\Delta\epsilon$ and $\lambda R^2/\mathcal{K}$ only. From these parameters, we computed the angle γ at which the curvature is zero defining an inflection point for the fold shape, as shown in Fig. 4d in the main text. In Fig. 4h in the main text, we plot the pairs (α, δ), and (γ, δ) for a single value of the dimensionless compressional rigidity $\lambda R^2/\mathcal{K}$, and compare it to experimental measurements without free parameters. In Fig. 4i in the main text, we plot the pairs $(\delta/R, P_B R^3/\mathcal{K})$ for a single value of the dimensionless compressional rigidity $\lambda R^2/\mathcal{K}$, and from the comparison with the experimental measurements, we find the best fit at the bending rigidity $\mathcal{K} \sim 0.5 \pm 0.2\,\mu N \cdot \mu$m.

Restoring force of indented elastic rings before buckling

In the following, we study the elastic forces of a system made of a spherical monolayer prior to folding that is adhered to the inner side of an spherical elastic capsule that is subjected to a normal force F_I, mimicking the effect of an indenter. Let us approximate the previous system by two concentric $3d$ elastic shells. The inner (outer) shell of radius R describes the tissue (alginate capsule), whose mechanical properties are characterized by the bending rigidity $\mathcal{K}$ ($\mathcal{K}^{cap}$) and the compressional rigidity λ (λ^{cap}).

The system deforms under the action of a small external point-like force F_I, which is localized and directed normal to the surface, forming a small bulge with radius $d = R\alpha$ and depth δ. This problem was addressed in (Landau and Lifshitz, 1975, Theory of elasticity) in the main text, and here, we restrict the analysis to $\alpha, \delta \ll 1$. At the bulge, the curvature of both surfaces scales as δ/d^2, and the total bending energy integrated over the deformed surface ($\propto d^2$) is $\sim (\mathcal{K} + \mathcal{K}^{cap})(\delta/d^2)^2 d^2$. Besides, the strain at the bulge area scales as $\sim \delta/R$ and the total stretching energy due to the external force is $\sim (\lambda + \lambda^{cap})(\delta/R)^2 d^2$. Therefore, the work generated by the external load $\sim F\delta$ is thus transformed into elastic deformations near the region where the force is applied. The shape of the bulge is given by the condition that the total mechanical energy

$$\mathcal{E} \sim (\mathcal{K} + \mathcal{K}^{cap})\left(\frac{\delta}{d^2}\right)^2 d^2 + (\lambda + \lambda^{cap})\left(\frac{\delta}{R}\right)^2 d^2 - F\delta \tag{S32}$$

is minimal, yielding the following relation for the minimal radius d and depth δ

$$d \sim \left(\frac{\mathcal{K} + \mathcal{K}^{cap}}{\lambda + \lambda^{cap}}\right)^{1/4} R^{1/2}, \tag{S33}$$

$$F \sim 4\sqrt{(\lambda + \lambda^{cap})(\mathcal{K} + \mathcal{K}^{cap})}\frac{\delta}{R}. \tag{S34}$$

In conclusion, prior to the buckling transition the response of the system subjected to a point-like force is a restoring force proportional to the displacement of the bulged region δ. Hence, let us define two spring constant:

$$K = 4\sqrt{(\lambda + \lambda^{cap})(\mathcal{K} + \mathcal{K}^{cap})}/R \tag{S35}$$

for capsules with unbuckled confluent monolayers and

$$K^{cap} = 4\sqrt{\lambda^{cap}\mathcal{K}^{cap}}/R = \sqrt{4/3}Eh^2/(1-\nu^2)R \tag{S36}$$

for capsules without tissues ($\mathcal{K} = \lambda = 0$).

To characterize the mechanical properties of epithelial tissues experimentally, we measure the linear regime of force-displacement curves by inducing small deformations with an indenter. Our findings permit to measure the spring constants under different configurations. In particular we compare the measured spring constant of capsules with and without tissues and we find that in general capsules are stiffer than the tissues underneath $\mathcal{K} \ll \mathcal{K}^{cap}$ and $\lambda \ll \lambda^{cap}$, meaning that the ratio between both coefficient can be approximated by

$$\frac{K}{K^{cap}} \sim 1 + \frac{1}{2}\left(\frac{\mathcal{K}}{\mathcal{K}^{cap}} + \frac{\lambda}{\lambda^{cap}}\right), \tag{S37}$$

a simple relation that permits to decipher the mechanics of tissues.

Section 5: Estimated parameters from the macroscopic approach

In this section, we summarize the main arguments used to determine the macroscopic parameters of epithelial monolayers that are bound to the inner surface of passive elastic shells in Table 1 in the main text.

The properties of alginate capsules are controlled externally. For the scale of tissue forces, alginate capsules behave as linear elastic materials with an elastic modulus $E = 19.5 \pm 0.7$ kPa for 2.5% alginate capsules (Fig. 3 in the main text) and a Poisson ratio $\nu = 1/2$. The typical thickness of the capsules is about $h = 19.9 \pm 0.4$ μm and their spherical shape has an inner radius of $R = 97 \pm 0.9$ μm. Since the thickness is smaller than the radius ($h \ll R$), capsules are approximated by elastic shells with a bending rigidity $\mathcal{K}^{cap} = Eh^3/(12(1-\nu^2)) = 17 \pm 1$ μN$\cdot\mu$m and a compressional rigidity $\lambda^{cap} = Eh/(1-\nu^2) = 0.52 \pm 0.02$ μN/μm, (Landau and Lifshitz, 1975, Theory of elasticity) in the main text. To estimate the macroscopic parameters of the monolayer, and in particular their bending and compressional rigidities ($\mathcal{K}$ and λ), we require an additional independent measurement that is provided by the shape and mechanics of folded tissues. On the one hand according to Fig. S6g-i, there is a one-to-one λ-independent relation between the opening angle α of a buckled elastic ring and the dimensionless force at the contact points $F_B R^2/\mathcal{K}$, as both are invertible functions. The latter is related to the pressure on the capsule by $P_B = F_B \cos\alpha/R$. As explained in the main text by fitting the curve between the fold height δ and the capsule pressure P_B, we obtain that the tissue bending rigidity is $\mathcal{K} = 0.5 \pm 0.2$ μN$\cdot\mu$m (see Fig. 4i in the main text), which is of the order of $\mathcal{K} \sim 10^8$ $k_B T$.

When a point-like force is applied on a capsule, it forms a small bulge whose restoring force is different whether the inner surface is coated with a tissue or not. The slope of the force displacement curve defines an effective spring constant. The measured spring constant for capsules is $K^{cap} \sim 0.064 \pm 0.003$ μN/μm (see Fig. 4j in the main text). When the spring constant is measured for capsules with a confluent tissue, its value rises slightly to $K \sim 0.074 \pm 0.007$ μN/μm (see Fig. 4j in the main text), suggesting that the monolayer resist the applied load.

Next, we use the ratio between $K/K^{cap} \sim 1.16 \pm 0.12$ (see Fig. 4j in the main text) to obtain from Eq. S37 that $\lambda/\lambda^{cap} \sim 0.28 \pm 0.24$ as $\mathcal{K}/\mathcal{K}^{cap} \sim 0.03 \pm 0.01$ was determined above. Therefore, the compressional rigidity is $\lambda = 0.15 \pm 0.13$ μN/μm for the value of λ^{cap} listed in Table 1 in the main text.

A scaling argument allows to estimate the order of magnitude of the pressure at buckling P_{buckling}. Let us consider that $\mathcal{K} \sim 1$ μN$\cdot\mu$m, $\lambda = 0.1$ μN/μm and $R \sim 100$ μm, so that the dimensionless number $\mathcal{K}/\lambda R^2 \sim 10^{-3} \ll 1$. The threshold of the excess strain at which the circular elastic ring buckles is $\Delta\epsilon_c \sim 10^{-1}$, where the numerical factor has been set to 10 in Eq. S21. By introducing this value to the relation between the pressure and the excess strain S25, we obtain that the pressure at buckling $P_{\text{buckling}} \sim 100$ Pa.

Section 6: Description of a confined elastic ring (microscopic approach)

We showed in (Merzouki, Malaspinas and Chopard, 2016, pp. 4745-4754; Merzouki et al, 2018, pp. 511-519) in the main text how simulated growing cell monolayers can fold in the absence of external constraints. We found that

the evolution of the cell monolayer morphology depends on the competition between the cell proliferation rate and the cell monolayer relaxation time. The cell mechanics affect directly the time needed by the cell monolayer to relax following a cell division, as well as the cell monolayer's geometry, which are discriminant characteristics of folded tissues. In this work, we extend this buckling study by investigating the growth of cell monolayers inside elastic environments. Our simulations are compared to experiments, where spherical cell monolayers are cultured inside hydrogel microcapsules.

Cell monolayer cross-section

A circular cell monolayer cross-section is modelled by a ring of quadrilateral cells. Each cell has two lateral edges, which separate it from its neighbour cells, as well as two boundary edges, corresponding to the basal and apical edges. A cell monolayer is characterised by the area elasticity of its cells, the elasticity of its cell edges and the bending rigidity between two neighbour cells. The energy function H of the cell monolayer cross-section is the following:

$$\begin{aligned} H = & \sum_{all\ cells\ \alpha} \frac{K_\alpha}{2}\Big(A_\alpha - A_\alpha^0\Big)^2 + \sum_{all\ edges\ e_{ij}} \frac{k_{i,j}^s}{2}\big(L_{i,j} - L_{i,j}^0\big)^2 \\ & + \sum_{all\ boundary\ edges\ e_{ij},e_{ik}} \frac{c^b}{2}\big(1 - \hat{\boldsymbol{N}}_{\boldsymbol{i,j}} \cdot \hat{\boldsymbol{N}}_{\boldsymbol{i,k}}\big)^2 \end{aligned} \tag{S38}$$

The first term of the energy represents the cell area elasticity. K_α and A_α^0 are the area elasticity coefficient and the preferred area of the cell α, respectively. In what follows, we set $K_\alpha = K = 10^9\ N/m^3$, (Merzouki, Malaspinas and Chopard, 2016, pp. 4745-4754; Merzouki et al, 2018, pp. 511-519) in the main text and $A_\alpha^0 = A^0 = 300\ \mu m^2$ for all the cells α. The second term models the elasticity of the cell edges. $k_{i,j}^s$ and $L_{i,j}^0$ are the spring coefficient along an edge e_{ij} and its preferred (resting) length, respectively. The higher $k_{i,j}^s$, the more resistant are the cell edges to deformation (extension/compression). This term prevents cells from adopting triangular shapes under lateral compression. In what follows, we set $L_{i,j}^0 = L^0 = \sqrt{A^0}$ for all edges e_{ij}. Finally, the third term stands for the bending rigidity of the cell monolayer, where c^b is the local bending rigidity coefficient. $\hat{\boldsymbol{N}}_{\boldsymbol{i,j}} \cdot \hat{\boldsymbol{N}}_{\boldsymbol{i,k}}$ is the dot product between the vectors $\hat{\boldsymbol{N}}_{\boldsymbol{i,j}}$ and $\hat{\boldsymbol{N}}_{\boldsymbol{i,k}}$. The latter are the unit vectors that are normal to the boundary (basal/apical) edges e_{ij} and e_{ik}. This energy term is minimised when the normal vectors of neighbour cells are parallel and the tissue curvature is null.

By deriving this energy function H with respect to a vertex position $\boldsymbol{r_i}$, we compute the internal force $\boldsymbol{F_i}$ applied on the vertex v_i.

$$\begin{aligned} \boldsymbol{F_i} = -\frac{dH}{d\boldsymbol{r_i}} \ = \ & -\frac{1}{2} \sum_{cell\ \alpha\ contains\ v_i} K_\alpha\Big(A_\alpha - A_\alpha^0\Big)\Big(\boldsymbol{ROT}(90^\circ) \cdot \big(\boldsymbol{r_{\alpha_{i-1}}} - \boldsymbol{r_{\alpha_{i+1}}}\big)\Big) \\ & - \sum_{all\ edges\ e_{ij}} k_{i,j}^s \frac{L_{i,j} - L_{i,j}^0}{l_{i,j}}\big(\boldsymbol{r_i} - \boldsymbol{r_j}\big) \\ & - \sum_{all\ boundary\ edges\ e_{ij},e_{ik}} c^b\big(1 - \hat{\boldsymbol{N}}_{\boldsymbol{i,j}} \cdot \hat{\boldsymbol{N}}_{\boldsymbol{i,k}}\big) \cdot \\ & \left(\frac{\big(\boldsymbol{r_i} - \boldsymbol{r_j}\big) + \big(\boldsymbol{r_i} - \boldsymbol{r_k}\big)}{L_{i,j} \cdot L_{i,k}} + \hat{\boldsymbol{N}}_{\boldsymbol{i,j}} \cdot \hat{\boldsymbol{N}}_{\boldsymbol{j,k}}\left(\frac{\boldsymbol{r_i} - \boldsymbol{r_j}}{\big(L_{i,j}\big)^2} + \frac{\boldsymbol{r_i} - \boldsymbol{r_k}}{\big(L_{i,k}\big)^2}\right)\right) \end{aligned} \tag{S39}$$

where

$$\boldsymbol{ROT}(\theta) = \begin{bmatrix} cos(\theta) & -sin(\theta) \\ sin(\theta) & cos(\theta) \end{bmatrix} \tag{S40}$$

is the rotation matrix in two dimensions, and $\boldsymbol{r_{\alpha_{i-1}}}$ and $\boldsymbol{r_{\alpha_{i+1}}}$ are the positions of the previous and next vertices, $v_{\alpha_{i-1}}$ and $v_{\alpha_{i+1}}$, of the vertex v_i in the cell α, when the vertices of α are ordered counterclockwise

Heterogeneous elastic capsules

We constrain the cell monolayer cross-section using an elastic ring environment with a spring coefficient k_{ring}.

This ring is characterised by its centre $\boldsymbol{c_{ring}}$. The ring could have a homogeneous shape and its geometry be solely characterised by a radius R_{ring}. However, for more realistic modelling of the experimental hydrogel micro-capsules, we actually constrain the growing cell monolayer cross-sections inside 'circular' elastic environments with heterogeneous borders. We perturb the circle radius with a set of sinusoidal signals. See Eq. (S41).

$$R_{ring}(\theta) = R^0_{ring} + \sum_{i=1}^{n} sin(\alpha_i \cdot \theta + \phi_i) \cdot A_i, \tag{S41}$$

where $R_{ring}(\theta)$ is the radius of the ring at an angle θ, n is the number of sinusoidal noises disturbing the initial radius of the ring R^0_{ring}, and α_i, ϕ_i and A_i are the frequency, phase and amplitude of the i^{th} sinusoidal perturbation.

The contact of the cells with the inner surface of the capsule yields a friction that restrains the movement of the cells. Cells are subjected to non-slipping forces along the capsule border. In our model, when a vertex v_i at a position $\boldsymbol{r_i}$ is close to the border of the capsule, $||\boldsymbol{r_i} - \boldsymbol{c_{ring}}|| > R_{ring}(\theta_i) - \epsilon$, it is subjected to a force that resists its tangential force component F_i^{tan} up to a given force threshold F_{NS}, where the subscript NS stands for "Non-Slipping". In contrast, when the vertex is far from the capsule border or when its tangential force component F_i^{tan} exceeds the non-slipping force threshold F_{NS}, then the vertex is free from the non-slipping force exerted along the capsule's surface.

Section 7: Folding quantification

For each simulation, the contour of the confining capsule is stored as well as the basal contour of the cell monolayer over time. The contours are stored in .csv files. Each line contains the (X, Y) coordinates of a point along the contour. Points are ordered counter-clockwise. The basal contour of the cell monolayer is defined by the counter-clockwise sequence of basal vertices v_i, at positions $\boldsymbol{r_i} = (x_i, y_i)$, along the cell monolayer cross-section. The dynamics of the cell monolayer can then be followed over time.

From the sequence of vertex positions $\boldsymbol{r_i} = (x_i, y_i)$, we compute the radius $R_i = ||\boldsymbol{r_i} - \boldsymbol{c_{ring}}||$ of each vertex (distance to the capsule center $\boldsymbol{c_{ring}}$) and its angle θ_i along the cell monolayer contour. The first characteristic property of a fold is its detachment from its initial unfolded configuration and its displacement from the border to the interior of the capsule. In order to identify a detachment, we compute the difference between a given contour profile $R(\theta)$ and the reference profile $R_{ref}(\theta)$; $dist(\theta) = R(\theta) - R_{ref}(\theta)$. The reference profile corresponds to the initial unfolded profile subjected to the confinement constraints. When the tissue detaches from the capsule and moves inward, the distance $dist(\theta)$ to the reference profile in this region is negative; $dist(\theta) < 0$. In contrast, when $dist(\theta) > 0$, this corresponds to a tissue that pushes outward on its confining environment. Because the number of cells (and vertices) of the growing simulated tissue evolves over time, the comparison between the tissue profiles requires a pre-processing. All the profiles are first interpolated to get their radius at specific angles $\theta \in]0, 2\pi]$.

The identification of detachments along the tissue contour starts with finding the local minima of the distance function with respect to the angle $dist = f(\theta)$. In order to ignore noises and minor detachments, we set a threshold ϵ_{dist}, ex. $\epsilon_{dist} = -10\mu m$, above which a local minimum is dismissed. The second step aims at delimiting the detachment, i.e. finding its start and end points. From each significant distance local minimum, we look backward and forward along the tissue contour for points with $dist \approx 0$, ex. $dist > -1\mu m$. These start and end points allow us to compute the width of the detachment. Moreover, the position of a detachment is computed as the mean position between the start and end points delimiting the detachment. In case different distance local minima have the same start and end points, they are considered as potential folds being part of a unique detachment.

There, we distinguish between a detachment and a fold. The fold delimitation is not solely based on the distance to the reference contour, but it is also characterised by an increased local curvature. The local curvature is the second derivative of the distance function $dist = f(\theta)$. In summary, a fold is characterised by a distance to the capsule and a curvature which exceed given thresholds ϵ_{dist} and ϵ_{curv}, respectively. In what follows, we use $\epsilon_{dist} = -10\mu m$ and $\epsilon_{curv} = 5e^{-4}$. The start and end points of a fold are the points along the contour (before and after the fold position) where the first and second derivatives of the distance change sign.

Section 8: Simulations and results

Effect of cell mechanics on buckling

In this section, we show how different cell and tissue mechanical properties, namely the cell stiffness and the

tissue bending rigidity, affect the timing of tissue folding as well as the number, the width and the position of folds that form.

For this purpose, we simulate 45 cell monolayer cross-sections for a set of normalised parameters $(\bar{k^s}, \bar{c^b})$, where $\bar{k^s} = \frac{k^s}{KA^0}$ and $\bar{c^b} = \frac{c^b}{K(A^0)^2}$. For each couple of normalised parameters $(\bar{k^s}, \bar{c^b})$, we start with a relaxed ring of 40 cells. All the cells are assigned the same preferred area $A^0 = 300\ \mu m^2$ and an area elasticity coefficient $K = 10^9\ N/m^3$. The cell monolayer cross-section is confined inside an elastic heterogeneous ring, with $k_{ring} = 0.06\ N/m$ and a non-slipping force $F_{NS} = \overline{F_{NS}} K (A^0)^{3/2}$ with $\overline{F_{NS}} = 0.01$, which corresponds to $F_{NS} = O(10^{-8})\ N$. The radius of the heterogeneous ring is perturbed using $n = 5$ sinusoids with frequencies $\alpha_i = i, \forall i = 1..n$, random amplitudes $A_i \in]0...0.02 \cdot R]$ and random phases $\phi_i \in]0...2\pi]$. Fig. S7a presents the distribution of the number of folds forming after 40 cell divisions and the number of cells when the first fold appears for each set of normalised parameters $(\bar{k^s}, \bar{c^b})$.

We observe that higher bending rigidity $\bar{c^b}$, which increases the differential tension between the boundary and the lateral cell edges, enhances cell monolayer thickening and therefore postpones and reduces tissue folding. In contrast, higher cell stiffness $\bar{k^s}$, which resists cell compression, accelerates and enhances tissue folding in response to cell proliferation.

In Fig. S7a, we highlight in red the histograms matching the experimental observations, i.e. a majority of 2 folds formation, followed by cases where 1 fold is observed, then fewer cases displaying 3 folds. This parameter region corresponds to a first fold forming at approximately 70 cells and an average cell aspect ratio at buckling $AR = 2 - 2.5$, while regions with larger bending rigidity show a postponed buckling when cells are much more elongated ($AR = 3 - 6$). We found that along the line $\bar{k^s}/\bar{c^b} = 0.1$, the fold number (Fig. S7a) was similar to experiments (see Fig. 5 in the main text).

The forces applied by the tissue on the capsule (and the other way around, the external forces applied by the capsule on the tissue) over time were monitored during our simulations. The evolution of the estimated pressure over time are presented in Fig. S7b. Experimentally, the force applied by the growing tissue on the capsule at buckling is estimated to be in the order of the micronewton $O(\mu N)$ ($F = 0.4 - 4\ \mu N$), and the pressure to be in the order $O(0.1\ kPa)$. In the highlighted regions of the model parameters (matching the experimental distribution of the number of forming folds), the first folds appear in our simulated tissues when the number of cells reaches $\approx 60 - 70$. In this time interval, the force applied by the simulated tissue cross-section on its elastic environment $F_{ext}^{CS} = \sum_i ||F_{ext}^i||$ varies between $0.5\ \mu N - 1\ \mu N$. The force F_{ext}^{CS} is the sum of all the external force norms applied by the tissue cross-section on the capsule. In 3D, we estimate the force applied by the spherical tissue F_{ext}^{SP} on the capsule to be:

$$F_{ext}^{SP} = \frac{F_{ext}^{CS} \cdot nbCells^{CS}}{\pi} \tag{S42}$$

Therefore, the pressure P at buckling in our simulations is computed as $P = \frac{F_{ext}^{SP}}{S}$, where $S = 4\pi R^2$ is the surface of the sphere with radius R. In our simulations, $R \approx 100 \mu m$. Experimentally, the capsule radius varies between $75 \mu m$ and $175 \mu m$, which corresponds to a $150 \mu m - 350 \mu m$ diameter. Finally, with approximately 70 cells at buckling, and a force applied by the tissue cross-section F_{ext}^{CS} between $0.5\ \mu N$ and $1\ \mu N$, we estimate that the pressure at buckling in our simulations to be $P \approx 0.17\ kPa$ for values of $k^s \sim 3 * 10^{-3}\ \mu$N/$\mu$m and $c^b \sim 9\ \mu$N$\cdot\mu$m Fig. S7b. This is consistent with the experimental pressure in the order of $0.1\ kPa$ estimated when the cultured cell monolayers buckle inside the elastic microcapsule.

Effect of confining environment

The non-slipping forces applied by the capsule on the cells play an important role on the timing, the number and the shape of the folds that form. We analysed the folding of simulated cell monolayers growing inside capsules with normalised non-slipping forces $\overline{F}_{NS} = \frac{F_{NS}}{K(A^0)^{3/2}}$ varying between 0.001 and 0.01.

We found that an increased friction between the capsule's inner surface and the cell monolayer leads to accelerated folds formation. More folds appear and they present wider shapes. In general, once a fold forms, the lateral cell compression in this region decreases. Without friction, the cells around the fold migrate into the fold, leading to the constriction of the fold's neck and the formation of a highly curved inward bud. In contrast, increased non-slipping forces prevent the migration of the cells into the fold that just formed. Therefore, the fold grows wider, other parts of the cell monolayer keep on accumulating lateral compressive stress due to cell proliferation, and additional folds form. Click here to watch the video, or follow the link: `https://youtu.be/C73R6kLNfQk`.